Giant Magnetochiral Anisotropy in Weyl Semimetal math xmlns="http://www.w3.org/1998/Math/MathML" display="inline">mrow>msub>mrow>mi>WTe/mi>/mrow>mrow>mn>2/mn>/mrow>/msub>/mrow>/math> Induced by Diverging Berry Curvature

Tomoyuki Yokouchi, Yuya Ikeda, Takahiro Morimoto, and Yuki Shiomi

Phys. Rev. Lett. **130**, 136301 — Published 30 March 2023

DOI: 10.1103/PhysRevLett.130.136301

Giant Magnetochiral Anisotropy in Weyl-semimetal WTe_2 Induced by Diverging Berry Curvature

Tomoyuki Yokouchi[1†], Yuya Ikeda[2], Takahiro Morimoto[2], and Yuki Shiomi[1]

[1] *Department of Basic Science, The University of Tokyo, Tokyo 152-8902, Japan*

[2] *Department of Applied Physics, The University of Tokyo, Tokyo 113-8656, Japan*

† To whom correspondence should be addressed. E-mail: yokouchi@g.ecc.u-tokyo.ac.jp

Abstract

The concept of Berry curvature is essential for various transport phenomena. However, an effect of the Berry curvature on magnetochiral anisotropy, i.e. nonreciprocal magneto-transport, is still elusive. Here, we report the Berry curvature originates the large magnetochiral anisotropy. In Weyl-semimetal WTe_2, we observed the strong enhancement of the magnetochiral anisotropy when the Fermi level is located near the Weyl points. Notably, the maximal figure of merit $\bar{\gamma}$ reaches 1.2×10^{-6} $m^2T^{-1}A^{-1}$, which is the largest ever reported in bulk materials. Our semiclassical calculation shows that the diverging Berry curvature at the Weyl points strongly enhances the magnetochiral anisotropy.

Whether physical responses are allowed or prohibited is closely related to symmetries [1]. For example, in the linear response regime, the anomalous Hall effect is allowed when time reversal symmetry is broken [2]. In contrast, spin Hall effect is allowed independent of both time reversal and crystalline symmetries [2]. In the nonlinear response regime, a nonlinear Hall effect without external magnetic field is allowed in a bilayer WTe_2 but prohibited in a bulk WTe_2 due to the difference in the crystalline symmetries between them [3,4]. In addition, the bulk photovoltaic effect, a nonlinear optical phenomenon, is allowed in system without spatial inversion symmetry [4, 5, 6]. Beyond the symmetry argument, the microscopic mechanisms of these physical phenomena have been intensively studied. An important finding is that the notion of the Berry curvature of electronic wave function is essential for the description of these phenomena [8]. For example, the intrinsic anomalous and spin Hall effects are proportional to the integral of Berry curvature over the Fermi sea [2]. In addition, recently, it is found that the Berry curvature also manifests itself in nonlinear responses; the nonlinear Hall effect under time reversal symmetry is induced by the dipole moment of the Berry curvature [3,4,9,10]. In one of the microscopic mechanisms of the bulk photovoltaic effect (shift current mechanism), photocurrent is quantified by the difference in the Berry connection between valance and conduction bands [11, 12]. Hence, investigating relationship between the Berry curvature and a physical response has been one of the central issues in modern condensed matter physics.

Only when the time reversal and spatial inversion symmetries are simultaneously broken, another class of the nonlinear responses is allowed, that is the magnetochiral anisotropy effect [13, 14, 15, 16, 17, 18, 19, 20, 21, 22, 23, 24, 25, 26, 27, 28, 29, 30, 31] which we focus on here. The magnetochiral anisotropy effect (also called the nonreciprocal magneto-transport effect) is nonreciprocal transport responses triggered by an external magnetic field; under magnetic fields, the longitudinal and transverse resistivity of a material is different for electric current I flowing to the right ($+I$) and to the left ($-I$). The magnetochiral anisotropy effect essentially differs from the nonlinear Hall effect, since the former requires time-reversal symmetry breaking but the latter does not. Hence physical mechanisms different from the nonlinear Hall effect must exist in the magnetochiral anisotropy effect. So far several underlying mechanisms of the magnetochiral anisotropy effect have been clarified. For example, an asymmetric electron scattering [18, 19, 22, 23, 31] and the magnetic-field-induced deformation of the Fermi surface caused by the Zeeman term [17, 20] have been identified as the microscopic mechanisms. From the viewpoint of symmetry, modification of electron motion due to the Berry curvature is also expected to affect the magnetochiral anisotropy effect, since the momentum-integrated Berry curvature can be nonzero in systems with broken time-reversal symmetry. However, the role of the Berry curvature on the magnetochiral anisotropy effect has not been well explored.

To study the effect of Berry curvature on the magnetochiral anisotropy effect, Weyl semimetals with broken spatial inversion symmetry [32, 33] are a suitable candidate. Weyl semimetals are quantum materials characterized by topologically nontrivial band structure and possess pairs of band crossing points termed Weyl points. The Weyl points act as monopoles of the Berry curvature, and the Berry curvature becomes singular and diverges at the Weyl points. Hence, when the Fermi level is located near the Weyl points, the effect of the Berry curvature is maximized and thus the magnetochiral anisotropy effect is expected to be dramatically enhanced. In this paper, we demonstrate this scenario using bulk crystals of a polar Weyl semimetal WTe_2. The symmetry of bulk WTe_2 is a $Pmn2_1$ (polar), and WTe_2 possesses four pairs of Weyl points [34,35,36]. Around the Weyl points, the Berry curvature is strongly enhanced as schematically shown in Fig. 1(a).

Generally, the direction of the electric field generated in the magnetochiral anisotropy effect depends on the magnetic field direction [13]. The presence of the mirror plane in WTe_2 constrains the expected direction of the voltage drop induced by the magnetochiral anisotropy responses in WTe_2 as shown in Figs. 1(b) and (c); the longitudinal response (hereafter called nonreciprocal magnetoresistance) is proportional to $\sin\theta$ and largest when the magnetic field (H) is perpendicular to the current. Here, θ is the relative angle between the magnetic-field direction and the current direction. In contrast, the transverse response (hereafter called second-harmonic Hall effect) is proportional to $\cos\theta$ and largest when H is parallel to the current. Here, we note although the nonreciprocal magnetoresistance was reported in nanometre-thick WTe_2 whose Fermi level is apart from the Weyl points [20], both the nonreciprocal magnetoresistance and the second-harmonic Hall effect have not been well investigated when the Femi level is tuned near the Weyl points hosting diverging Berry curvature.

In Figs. 1(d) and (e), we present the magnetic-field dependence of the second-harmonic Hall effect and the nonreciprocal magnetoresistance in bulk WTe_2 whose Fermi level is close to the Weyl points (sample F). Here, we evaluate the Fermi level position from the carrier densities of electrons and holes obtained by the Hall resistivity measurement (see [37] for details). Because the magnetochiral anisotropy effect is proportional to the magnitude of the square of the current density j^2, we measured the second harmonic longitudinal and transverse resistivity ($\rho_{xx}^{2\mathrm{f}}$ and $\rho_{yx}^{2\mathrm{f}}$) (see also [37] for details). In accord with the expected contribution from the magnetochiral anisotropy effect, the field profiles of $\rho_{xx}^{2\mathrm{f}}$ and $\rho_{yx}^{2\mathrm{f}}$ are anti-symmetric against the magnetic field. Here, $\rho_{xx}^{2\mathrm{f}}$ and $\rho_{yx}^{2\mathrm{f}}$ are anti-symmetrized with respect to the magnetic field (see also [37]). The field profiles of the nonreciprocal magnetoresistance and the second-harmonic Hall effect before anti-symmetrization [$\rho_{xx,\mathrm{meas.}}^{2\mathrm{f}}(H)$ and $\rho_{yx,\mathrm{meas.}}^{2\mathrm{f}}(H)$] is also anti-symmetric against the magnetic field as shown in Fig. S5 [37]. The magnitude of the magnetochiral anisotropy can be represented by $\bar{\gamma}_{xx}$ and $\bar{\gamma}_{yx}$, which are independent of the sample size and defined by $E_x^{\mathrm{MCA}} = \rho_{xx}\bar{\gamma}_{xx}Bj^2$ and $E_y^{\mathrm{MCA}} = \rho_{xx}\bar{\gamma}_{yx}Bj^2$, respectively. Here, $\boldsymbol{E}^{\mathrm{MCA}}$ is the magnetochiral anisotropy electric field, and $\bar{\gamma}_{xx}$ and $\bar{\gamma}_{yx}$ are related to $\rho_{xx}^{2\mathrm{f}}$ and $\rho_{yx}^{2\mathrm{f}}$ as $\bar{\gamma}_{xx} = -2\rho_{xx}^{2\mathrm{f}}/(\rho_{xx}jB)$ and $\bar{\gamma}_{yx} = -2\rho_{yx}^{2\mathrm{f}}/(\rho_{xx}jB)$ [37]. The obtained magnitudes of $|\bar{\gamma}_{yx}|$ and $|\bar{\gamma}_{xx}|$ are as large as 1.2×10^{-6} $\mathrm{m^2T^{-1}A^{-1}}$ and 0.34×10^{-6} $\mathrm{m^2T^{-1}A^{-1}}$ at 1 T, respectively. Remarkably, $\bar{\gamma}_{yx}$ is much larger than previously reported $\bar{\gamma}_{yx}$ values in bulk materials [42] and $\bar{\gamma}_{xx}$ is almost identical to the previously reported largest value of $\bar{\gamma}_{xx}$ in $ZrTe_5$ [29]. Interestingly, the second-harmonic Hall effect (i.e. $\rho_{yx}^{2\mathrm{f}}$ for H // I) is larger than the nonreciprocal magnetoresistance (i.e. $\rho_{xx}^{2\mathrm{f}}$ for $H \perp I$) [Figs. 1(d) and (e)]. This feature cannot be explained by the previously reported asymmetric electron scattering mechanism, in which the magnitude of the second-harmonic Hall effect and the nonreciprocal magnetoresistance must be the same [19]. As will be discussed later, this difference originates from the effects of the Berry curvature and the chiral anomaly.

To further confirm that the observed signals originate from the magnetochiral anisotropy effect, first, we investigated the dependence of $\rho_{yx}^{2\mathrm{f}}$ with H // I on the input-current frequency (f) and on the current density (j) in sample A. The Fermi level of sample A is also located near the Weyl points as in sample F. As expected in the second-harmonic Hall effect, the magnitude of $\rho_{yx}^{2\mathrm{f}}$ is independent of f and linearly increases with increasing j in the low current density region [Figs. 2(a) and (c)]. Note that the deviation from the linear relationship in Fig. 2(c) at high current is attributed to the temperature increase due to the Joule heating effect; the maximum temperature increase is approximately 5 K [Fig. 2(b)], which is estimated from the change in the linear longitudinal resistivity. Then, we investigated polarity-direction dependence; the sign of the second-harmonic Hall effect and the nonreciprocal magnetoresistance should be reversed when the polarity direction is reversed [13]. We divided a WTe_2 sample into two (samples D and L) so that the polarity directions are opposite to each other [Fig. 2(d)]. As shown in Figs. 2(e)-(h), the signs of $\rho_{yx}^{2\mathrm{f}}/\rho_{xx}$ and $\rho_{xx}^{2\mathrm{f}}/\rho_{xx}$ are opposite for samples D and L in accord with the expected trends in the second-harmonic Hall effect and the nonreciprocal magnetoresistance. We also measured $\rho_{yx}^{2\mathrm{f}}/\rho_{xx}$ as a function of the relative angle (θ) between the magnetic-field direction and the current direction. As shown in Fig. 3(a), $\rho_{yx}^{2\mathrm{f}}/\rho_{xx}$ obeys $\cos\theta$ as expected. These results corroborate that the observed signals originate from the magnetochiral anisotropy effect. In addition, as a crosscheck, we reproduced the magnetochiral anisotropy in dc measurements [37]

Then, we investigate the temperature dependence of the second-harmonic Hall effect and the nonreciprocal magnetoresistance. In Figs. 3(b) and (c), we show the temperature dependence of $|\sigma_{xyy}|$ and $|\sigma_{xxx}|$ at 1 T for sample A and sample F. Here, σ_{xyy} and σ_{xxx} are defined as $j_x = \sigma_{xyy}E_y^2B$

and $j_x = \sigma_{xxx} E_x^2 B$ and related to $\rho_{yx}^{2\mathrm{f}}$ and $\rho_{xx}^{2\mathrm{f}}$ as $\sigma_{xxx} = -2\rho_{xx}^{2\mathrm{f}} j / B\rho_{xx}^3$ and $\sigma_{xxx} = 2\rho_{yx}^{2\mathrm{f}} j / B\rho_{xx}^3$, respectively [37]. As can be seen from Figs. 3(b) and (c), the absolute values of σ_{xyy} and σ_{xxx} increase notably with decreasing temperature. The enhancement at low temperatures should be closely related to the microscopic mechanism and will be discussed later.

Next, we investigated the Fermi level dependence of the second-harmonic Hall effect and the nonrecirpcal mangetoresistance. In WTe_2, it is known that the Fermi level position changes due to a deficiency of Te and can be evaluated by the ratio between the hole carrier density (n_h) and the electron carrier density (n_e) [43] . According to the previous study [43], when the Fermi level is close to the Weyl points, $n_\mathrm{e}/n_\mathrm{h}$ is approximately 1.08. Hence, we measured $\bar{\gamma}_{yx}$ and $\bar{\gamma}_{xx}$ in more than ten samples and plot the absolute value of $\bar{\gamma}_{yx}$ and $\bar{\gamma}_{xx}$ at 1 T as a function of $n_\mathrm{e}/n_\mathrm{h}$ (see also [44] and [37] for the evaluation of n_e and n_h). As shown in Figs. 4(a) and (b), $|\bar{\gamma}_{yx}|$ and $|\bar{\gamma}_{xx}|$ systematically depend on $n_\mathrm{e}/n_\mathrm{h}$ or equivalently the Fermi level position. Notably, both $|\bar{\gamma}_{yx}|$ and $|\bar{\gamma}_{xx}|$ change by more than four orders of magnitude and are largest when the Fermi level is close to the Weyl points. We note that this Fermi level dependence of $|\bar{\gamma}_{yx}| = |\rho_{yx}^{2\mathrm{f}}|/\rho_{xx}$ and $|\bar{\gamma}_{xx}| = |\rho_{xx}^{2\mathrm{f}}|/\rho_{xx}$ mainly results from that of $\rho_{yx}^{2\mathrm{f}}$ and $\rho_{xx}^{2\mathrm{f}}$; as shown in Fig. S9 [37], ρ_{xx} is almost independent of the Fermi level position. The observed substantial increase in the magnetochiral anisotropy responses around the Weyl points cannot be explained by the previously reported semiclassical calculation of the nonreciprocal responses in WTe_2 [20], in which an effect of the Berry curvature is not included; in this previous work, the ratio of the change in the calculated nonreciprocal response is less than 10 as a function of the Fermi level position.

The observed Fermi-level dependence of the magnetochiral anisotropy effect can be understood by a semiclassical treatment of current responses including the contribution from the Berry curvature. We use Boltzmann equation to derive momentum distribution under the electric field and the magnetic field and calculate the second-harmonic Hall and nonreciprocal magnetoresistance responses (for detail, see [37]). We find that the combination of C_2 rotation symmetry of WTe_2 around the z direction and the time reversal symmetry leads to a constraint that the transverse nonlinear conductivity σ_{xyy} and longitudinal nonlinear conductivity σ_{xxx} is proportional to the square of the relaxation time τ. The semiclassical treatment shows that such τ^2 contribution to the second-harmonic Hall current arises from energy shift due to orbital magnetic moment and the momentum shift related to chiral anomaly. These effects are substantially enhanced when the Fermi energy is close to the Weyl point reflecting the diverging Berry curvature around the Weyl point. Therefore, as shown in Figs. 4(c) and (d), large second-harmonic Hall and nonreciprocal magnetoresistance responses appear when the Fermi energy is tuned close to the Weyl points, which is qualitatively consistent with the observed enhancement of the second-harmonic Hall effect and the nonreciprocal magnetoresistance. In particular, when the Fermi energy is located between the Weyl and anti-Weyl points, the contribution from the two nodes add up in a constructive way, leading to giant magnetochiral anisotropy.

Our theory can also explain the experimentally observed difference in the magnitudes of the second-harmonic Hall effect and the nonreciprocal magnetoresistance. As already shown in Figs. 1(d) and (e), the magnitude of the second-harmonic Hall effect is larger than that of the nonreciprocal magnetoresistance in sample F. Furthermore, all other samples also have the same relationship regardless of the current direction with respect to the crystalline axis; as presented in Figs. 4(a) and (b), the magnitude of the second-harmonic Hall effect is larger than that of the nonreciprocal magnetoresistance for each sample. In the theory, as can be seen from Eq. S11 [37], the second order current contains the $\boldsymbol{E} \cdot \boldsymbol{B}$ term that originates from the chiral anomaly [45, 46]. Since the $\boldsymbol{E} \cdot \boldsymbol{B}$ term is largest for $j \parallel B$ (the second-harmonic Hall configuration) and zero for $j \perp$ B (the nonreciprocal magnetoresistance configuration), the second-harmonic Hall effect is always larger than the nonreciprocal magnetoresistance, if the Fermi level position is the same. Furthermore, the present theory is also consistent with the experimentally observed temperature dependence of σ_{xyy} and σ_{xxx};

both σ_{xyy} and σ_{xxx} increase with decreasing temperature [see Figs. 3(b) and (c)]. Since σ_{xyy} and σ_{xxx} in our theory are proportional to the square of the relaxation time, they should increase with decreasing temperature because of the enhancement of the relaxation time τ at low temperatures.

We note that, in our discussion, the effect of the surface states of WTe_2 [47] is negligible; due to the spatial inversion symmetry breaking at the surfaces, the magnetochiral anisotropy is allowed at the surface states. However, in the case of bulk samples, the magnetochiral anisotropy at the top and bottom surfaces is cancelled out because their polarity is opposite. Moreover, as shown in Fig. S10 [37], $|\bar{\gamma}_{yx}|$ is independent of the sample thickness, which also supports that the observed signals are irrelevant to the surface state. We also note that both theoretically calculated and experimentally observed magnetochiral anisotropy exhibits nonlinear B dependence in the high field region [Fig. S1(c) [37]]. This is probably due to the magnetic-field induced Fermi surface deformation. While the magnetic field dependence in the high field region is not accurately reproduced by the theoretical calculation [37], this discrepancy probably results from the simplified band structure in the theoretical calculation. Hence, in the comparison between the theoretical and experimental results, we estimated the magnitude of the magnetochiral anisotropy in the low field region.

To summarize, we observed the giant magnetochiral anisotropy effect when the Fermi level is close to the Weyl points. A semiclassical calculation of magnetochiral anisotropy responses indicates that the diverging Berry curvature at the Weyl points plays a crucial role in the observed enhancement of the magnetochiral anisotropy. Our finding demonstrates that the Berry curvature has a large impact on the magnetochiral anisotropy effect and is important for exploring large diode effects.

Acknowledgments

This works was supported by JST FOREST Program (Grant No. JPMJFR203H), JST PRESTO (Grant No. JPMJPR19L9), JST CREST (Grant No. JPMJCR19T3), JSPS KAKENHI (Grant Nos. 22H04464, 22H05449, 21K18890, 21H01794, 19H05600, and 19K14667), and Murata Science Foundation

References

1. R. R. Birss, Symmetry and Magnetism. (North-Holland Pub., Amsterdam, 1966).
2. N. Nagaosa, J. Sinova, S. Okada, A. H. MacDonald, and N. P. Ong, Anomalous Hall effect. Rev. Mod. Phys. **82**, 1539 (2010).
3. Q. Ma *et al*., Observation of the nonlinear Hall effect under time-reversal-symmetric conditions. Nature **565**, 337 (2019).
4. Z. Z. Du, H. Z. Lu, and X. C. Xie, Nonlinear Hall effects. Nat. Rev. Phys. **3**, 744 (2021).
5. I. Grinberg *et al*., Perovskite oxides for visible-light-absorbing ferroelectric and photovoltaic materials. Nature **503**, 509 (2013).
6. G. B. Osterhoudt *et al*., Colossal mid-infrared bulk photovoltaic effect in a type-I Weyl semimetal. Nat. Mater. **18**, 471 (2019).
7. Y. J. Zhang, T. Ideue, M. Onga, F. Qin, R. Suzuki, A. Zak, R. Tenne, J. H. Smet, and Y. Iwasa, Enhanced intrinsic photovoltaic effect in tungsten disulfide nanotubes. Nature **570**, 349 (2019).
8. D. Xiao, M-C. Chang and Q. Niu, Berry phase effects on electronic properties. Rev. Mod. Phys. **82**, 1959 (2010).
9. S. Lai *et al*., Third-order nonlinear Hall effect induced by the Berry-connection polarizability tensor. Nat. Nanotech. **16**, 869 (2021).
10. D. Kumar, C.-H. Hsu, R. Sharma, T.-R. Chang, P. Yu, J. Wang, G. Eda, G. Liang, and H. Yang, Room-temperature nonlinear Hall effect and wireless radiofrequency rectification in Weyl semimetal $TaIrTe_4$. Nat. Nanotechnol. **16**, 421 (2021).
11. S. M. Young and A. M. Rappe, First Principles Calculation of the Shift Current Photovoltaic Effect in Ferroelectrics. Phys. Rev. Lett. **109**, 116601 (2012).
12. T. Morimoto and N. Nagaosa, Topological nature of nonlinear optical effects in solids. Sci. Adv. **2**, e1501524 (2016).
13. Y. Tokura and N. Nagaosa, Nonreciprocal response from non-centrosymmetric quantum materials. Nat. Commun. **9**, 3740 (2018).

14. G. L. J. A. Rikken, J. Fölling and P. Wyder, Electrical Magnetochiral Anisotropy. Phys Rev. Lett. **87**, 236602 (2001).

15. F. Pop, P. Auban-Senzier, E. Canadell, G. L. J. A. Rikken, and N. Avarvari, Electrical magnetochiral anisotropy in a bulk chiral molecular conductor. Nat. Commun. **5**, 3757 (2014).

16. C. Avci, K. Garello, A. Ghosh, M. Gabureac, S. F. Alvarado, and P. Gambardella, Unidirectional spin Hall magnetoresistance in ferromagnet/normal metal bilayers. Nat. Phys **11,** 570 (2015).

17. T. Ideue, K. Hamamoto, S. Koshikawa, M. Ezawa, S. Shimizu, Y. Kaneko, Y. Tokura, N. Nagaosa, and Y. Iwasa, Nat. Phys. **13,** 578 (2017).

18. T. Yokouchi, N. Kanazawa, A. Kikkawa, D. Morikawa, K. Shibata, T. Arima, Y. Taguchi, F. Kagawa, and Y. Tokura, Electrical magnetochiral effect induced by chiral spin fluctuations. Nat. Commun. **8,** 866 (2017).

19. K. Yasuda, A. Tsukazaki, R. Yoshimi, K. Kondou, K. S. Takahashi, Y. Otani, M. Kawasaki, and Y. Tokura, Current-Nonlinear Hall Effect and Spin-Orbit Torque Magnetization Switching in a Magnetic Topological Insulator. Phys. Rev. Lett. **119**, 137204 (2017).

20. P. He, C.-H. Hsu, S. Shi, K. Cai, J. Wang, Q. Wang, G. Eda, H. Lin, V. M. Pereira, and H. Yang Nonlinear magnetotransport shaped by Fermi surface topology and convexity. Nat. Commun. **10,** 1290 (2019).

21. G. L. J. A. Rikken and N. Avarvari, Strong electrical magnetochiral anisotropy in tellurium. Phys. Rev. B **99,** 245153 (2019).

22. R. Aoki, Y. Kousaka, and Y. Togawa Anomalous Nonreciprocal Electrical Transport on Chiral Magnetic Order. Phys. Rev. Lett. **122**, 057206 (2019).

23. N. Jiang, Y. Nii, H. Arisawa, E. Saitoh, and Y. Onose, Electric current control of spin helicity in an itinerant helimagnet. Nat. Commun. **11**, 1601 (2020).

24. K. Yasuda, T. Morimoto, R. Yoshimi, M. Mogi, A. Tsukazaki, M. Kawamura, K. S. Takahashi, M. Kawasaki, N. Nagaosa, and Y. Tokura Large non-reciprocal charge transport mediated by quantum anomalous Hall edge states. Nat. Nanotechnol. **15,** 831 (2020).

25. F. Ando, Y. Miyasaka, T. Li, J. Ishizuka, T. Arakawa, Y. Shiota, T. Moriyama, Y. Yanase, and T. Ono, Observation of superconducting diode effect. Nature **584,** 373 (2020).

26. H. Narita *et al.*, Field-free superconducting diode effect in noncentrosymmetric superconductor/ferromagnet multilayers. Nat. Nanotechnol. **17**, 823 (2022).

27. F. Calavalle *et al.*, Gate-tuneable and chirality-dependent charge-to-spin conversion in tellurium nanowires. Nat. Mater. **21**, 526 (2022).

28. H. F. Legg *et al.*, Giant magnetochiral anisotropy from quantum-confined surface states of topological insulator nanowires. Nat. Nanotechnol. **17**, 696 (2022).

29. Y. Wang, H. F. Legg, T. Bömerich, J. Park, S. Biesenkamp, A. A. Taskin, M. Braden, A. Rosch, and Y. Ando, Gigantic Magnetochiral Anisotropy in the Topological Semimetal $ZrTe_5$. Phys. Rev. Lett. **128**, 176602 (2022).

30. L. Bauriedl *et al.*, Supercurrent diode effect and magnetochiral anisotropy in few-layer $NbSe_2$. Nat. Commun. **13**, 4266 (2022).

31. H. Ishizuka, and N. Nagaosa Anomalous electrical magnetochiral effect by chiral spin-cluster scattering. Nat. Commun. **11**, 2986 (2020).

32. N. P. Armitage, E. J. Mele, and A. Vishwanath, Weyl and Dirac semimetals in three-dimensional solids. Rev. Mod. Phys. **90,** 015001 (2018).

33. B. Q. Lv, T. Qian, and H. Ding, Experimental perspective on three-dimensional topological semimetals. Rev. Mod. Phys. **93**, 025002 (2021).

34. S. Kabashima, Electrical properties of tungsten-ditelluride WTe_2. J. Phys. Soc. Jpn. **21,** 945 (1966).

35. M. N. Ali *et al.*, Large, non-saturating magnetoresistance in WTe_2. Nature **514**, 205 (2014).

36. A. Soluyanov, D. Gresch, Z. Wang, Q.S. Wu, M. Troyer, X. Dai, and B. A. Bernevig, Type-II Weyl semimetals. Nature **527**, 495 (2015).

37. See the Supplemental Material for a description of the experimental method, theoretical calculations, and supplementary results, which includes Refs.[38-41].

38. T. Morimoto and N. Nagaosa, Chiral anomaly and giant magnetochiral anisotropy in noncentrosymmetric Weyl semimetals. Phys. Rev. Lett. **117**, 146603 (2016).

39. A. Zyuzin and A. Y. Zyuzin, Chiral anomaly and second-harmonic generation in Weyl semimetals. Phys. Rev. B 95, 085127 (2017).

40. T. Morimoto, S. Zhong, J. Orenstein, and J. E. Moore, Semiclassical theory of nonlinear magneto-optical responses with applications to topological Dirac/Weyl semimetals. Phys. Rev. B **94**, 245121 (2016).

41. M. N. Ali, L. Schoop, J. Xiong, S. Flynn, Q. Gibson, M. Hirschberger, N. P. Ong and R. J. Cava, Correlation of crystal quality and extreme magnetoresistance of WTe_2 EPL **110**, 67002 (2015).

42. T. Yokouchi, S. Hoshino, N. Kanazawa, A. Kikkawa, D. Morikawa, K. Shibata, T. Arima, Y. Taguchi, F. Kagawa, N. Nagaosa, and Y. Tokura, Current-induced dynamics of skyrmion strings. Sci. Adv. **4**, eaat1115 (2018).

43. Y. Y. Lv *et al*., Experimental Observation of Anisotropic Adler-Bell-Jackiw Anomaly in Type-II Weyl Semimetal $Wte_{1.98}$ Crystals at the Quasiclassical Regime. Phys. Rev. Lett. **118**, 096603 (2017).

44. T. Luo, H. Li, Y. M. Dai, H. Miao, Y. G. Shi, H. Ding, A. J. Taylor, D. A. Yarotski, R. P. Prasankumar, and J. D. Thompson, Hall effect in the extremely large magnetoresistance semimetal WTe_2. Appl. Phys. Lett. **107**, 182411 (2015).

45. J. Xiong, S. K. Kushwaha, T. Liang, J. W. Krizan, M. Hirschberger, W. Wang, R. J. Cava, and N. P. Ong, Evidence for the chiral anomaly in the Dirac semimetal Na_3Bi. Science **350**, 413 (2015).

46. M. Hirschberger, S. Kushwaha, Z. Wang, Q. Gibson, S. Liang, C. A. Belvin, B. A. Bernevig, R. J. Cava, and N. P. Ong, The chiral anomaly and thermopower of Weyl fermions in the half-Heusler GdPtBi. Nat. Mater. **15**, 1161 (2016).

47. P. Li, Y. Wen, X. He, Q. Zhang, C. Xia, Z.-M. Yu, S. A. Yang, Z. Zhu, H. N. Alshareef, and X.-X- Zhang, Evidence for topological type-II Weyl semimetal WTe_2. Nat. Commun. **8**, 2150 (2017).

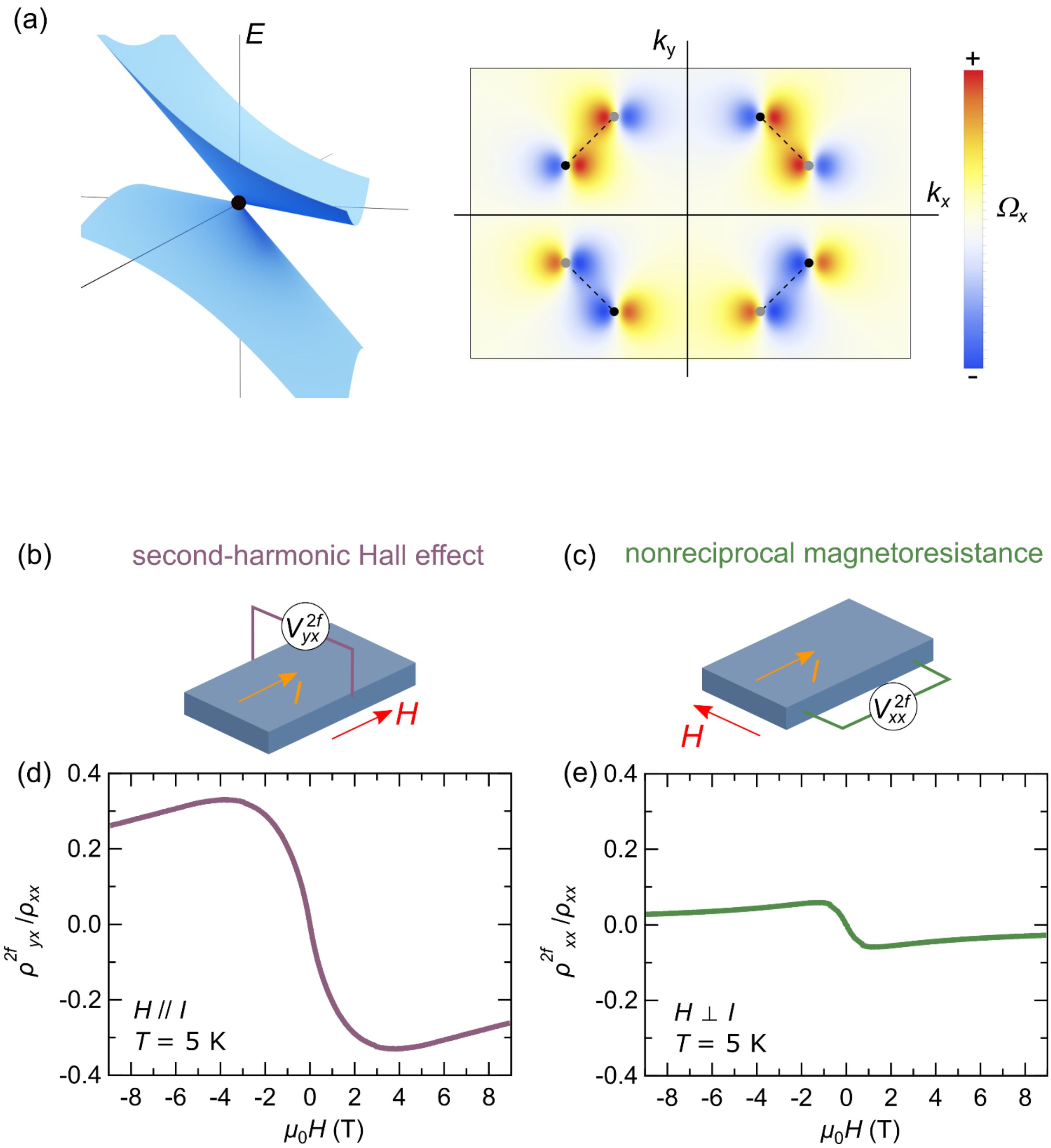

Fig. 1. (a) Schematics of the energy dispersion for a type-□ Weyl semimetal near a Weyl point and the Berry curvature (Ω_x) around the Weyl points in WTe_2. The black and grey circles represent Weyl points with the chirality η = +1 and -1, respectively. Experimental configurations for (b) the second-harmonic Hall effect and (c) the nonreciprocal magnetoresistance. Magnetic-field dependence of (d) the second-harmonic Hall effect and (e) the nonreciprocal magnetoresistance in sample F measured with j = 8.8×10^5 Am^{-2} and f = 33 Hz at 5 K. The current direction is parallel to the b-axis.

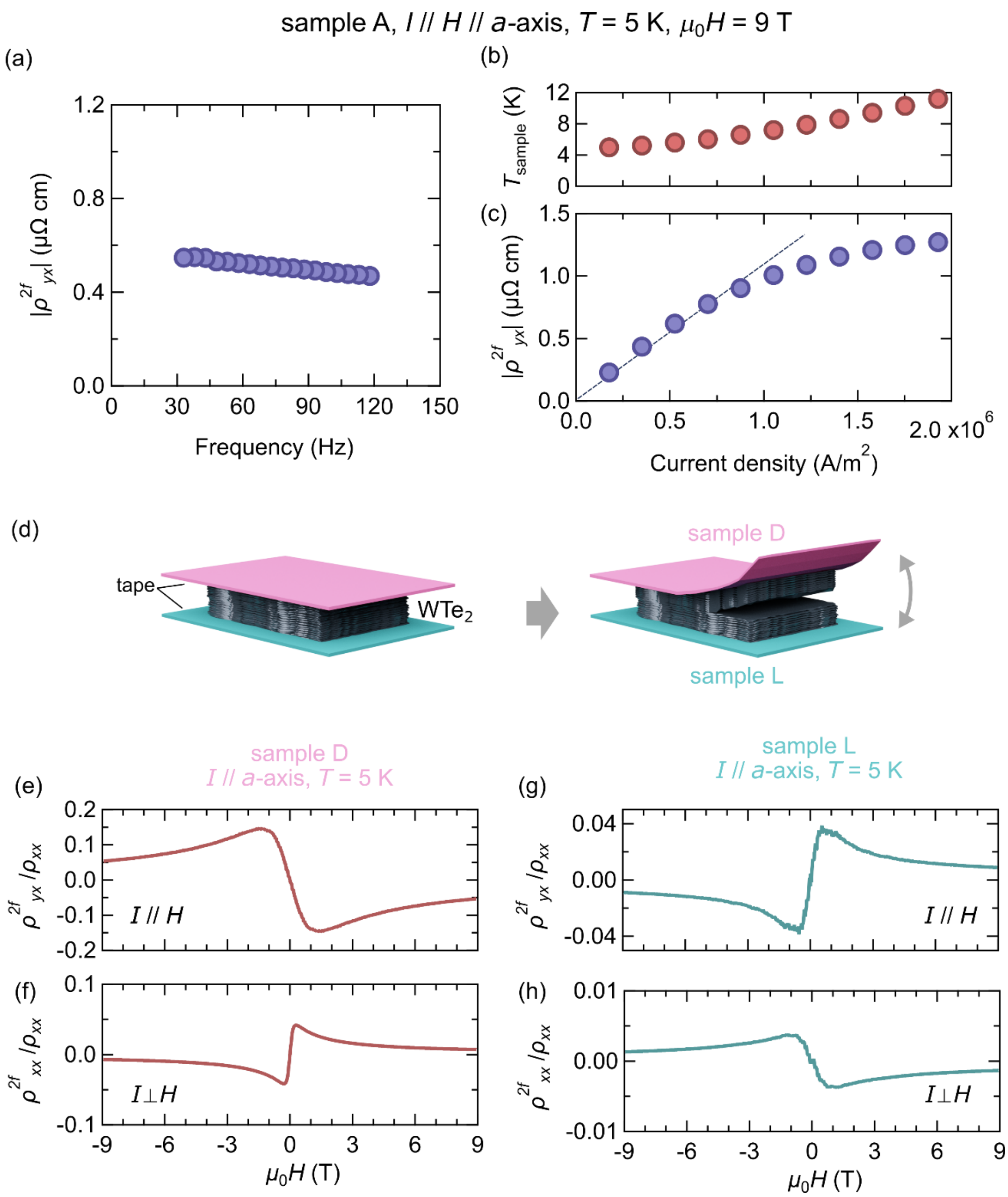

Fig. 2. (a) Frequency dependence of ρ_{yx}^{2f} and (b) current density dependence of the estimated temperature of the sample and (c) of ρ_{yx}^{2f} in sample A. The frequency dependence is measured with $j = 0.44\times10^{6}$ Am^{-2} and the current dependence is measured with $f = 53$ Hz. The current direction is parallel to the *a*-axis. (d) Schematic of the fabrication of samples D and L, in which the polarity directions are opposite to each other. (e)-(h) Magnetic-field dependence of the second-harmonic Hall effect in sample D and sample L and the nonreciprocal magnetoresistance in sample D and sample L measured with $j = 1.2\times10^{6}$ Am^{-2} and $f = 33$ Hz.

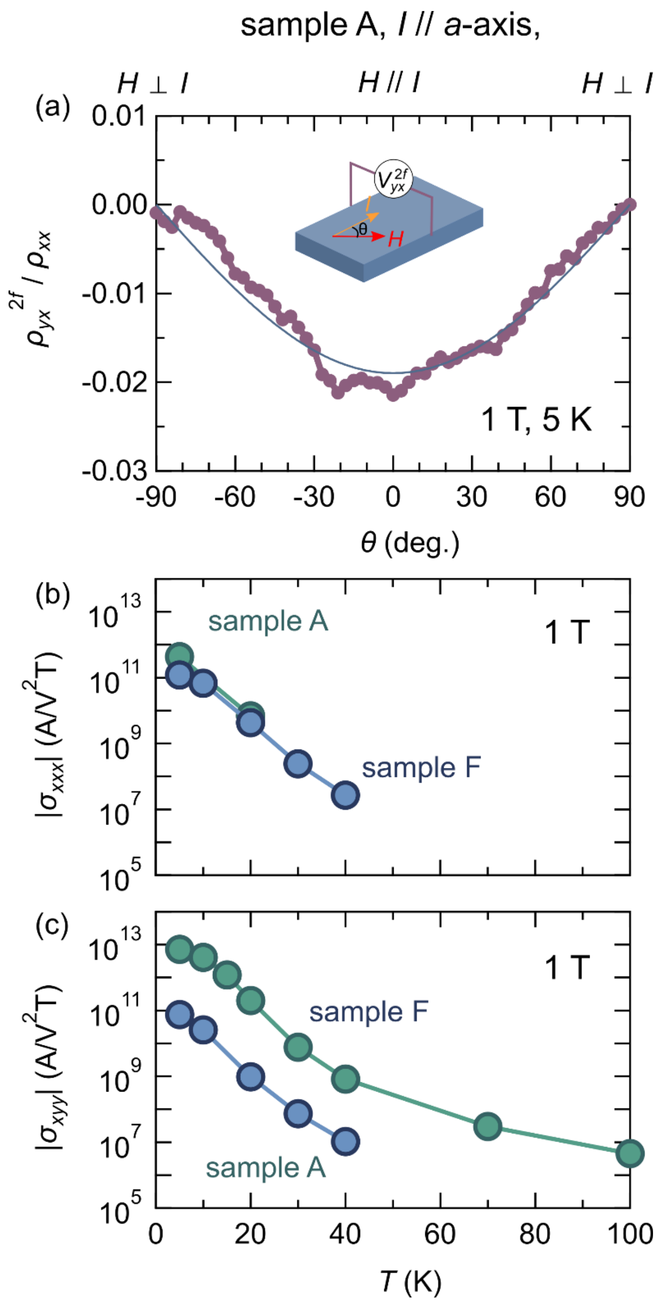

Fig. 3. (a) Angular dependence of $\rho_{yx}^{2\mathrm{f}}/\rho_{xx}$ measured with $j = 8.8\times10^5$ Am^{-2}, $f = 3.3$ Hz, and I // a-axis. The definition of θ is shown in the inset. The blue lines are fits to $\cos\theta$. (b), (c) Temperature dependence of $|\sigma_{xyy}| = 2|\rho_{yx}^{2\mathrm{f}}|j/\rho_{xx}^3 B$ and $|\sigma_{xxx}| = 2|\rho_{xx}^{2\mathrm{f}}|j/\rho_{xx}^3 B$ at 1 T in samples A and F. The current density for sample A and sample F is $j = 8.8\times10^5$ Am^{-2} and 3.4×10^5 Am^{-2}, respectively. The current direction is parallel to the a-axis in sample A and the b-axis in sample F. The frequency of the current is $f = 33$ Hz in both samples.

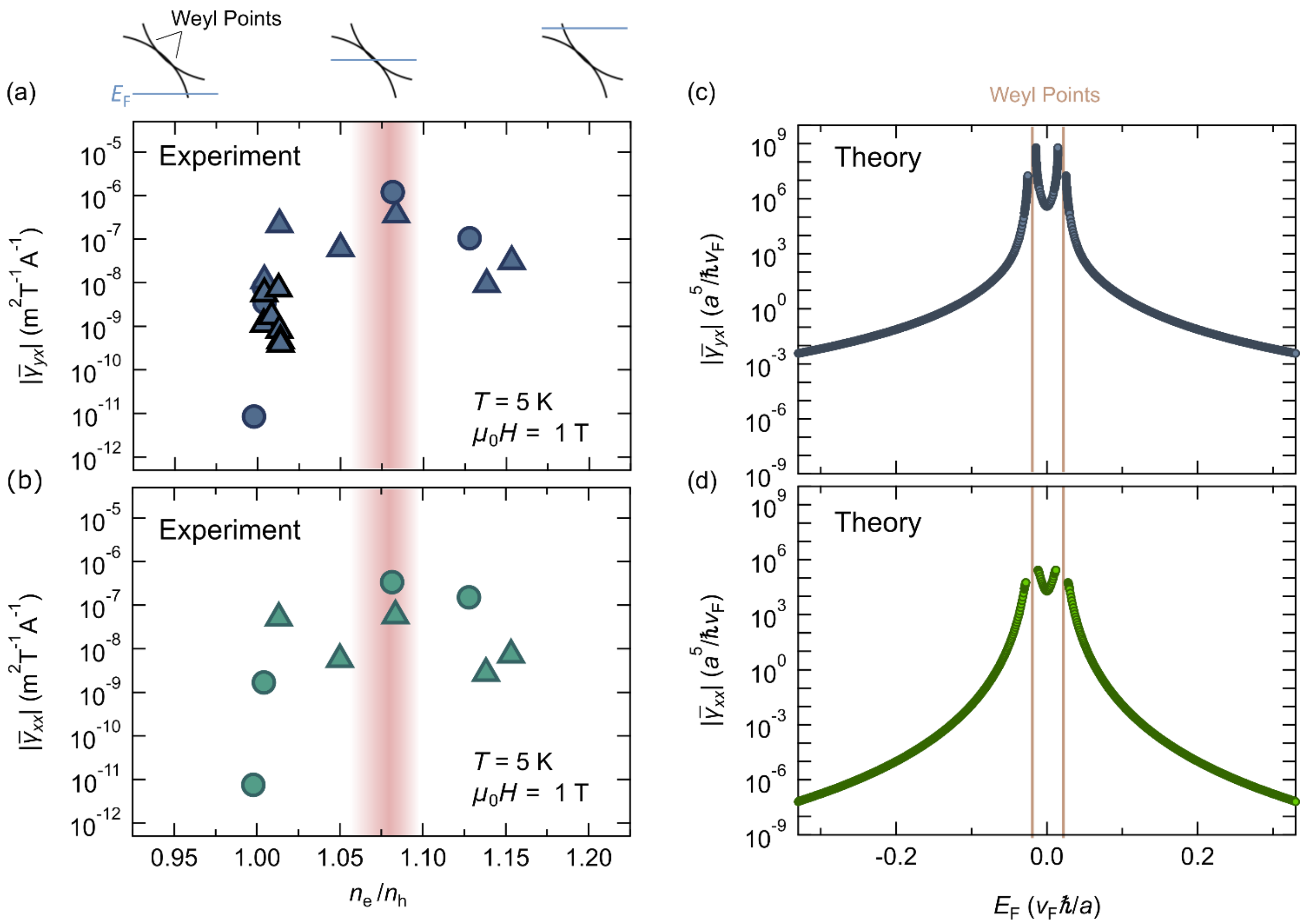

Fig. 4. (a), (b) Absolute values of $\bar{\gamma}_{yx} = 2\rho_{yx}^{2f}/\rho_{xx}\ jB$ and $\bar{\gamma}_{xx} = 2\rho_{xx}^{2f}/\rho_{xx}\ jB$ as a function of the ratio between electron carrier density (n_e) and hole carrier density (n_h). The circle and triangle points are samples measured with *I* // *b*-axis and *I* // *a*-axis, respectively. The upper panel schematically denotes the position of the Fermi level corresponding to the value of n_e/n_h. The region where the Fermi level is close to the Weyl points is denoted by the red shadow. (c), (d) Absolute values of $\bar{\gamma}_{yx}$ and $\bar{\gamma}_{xx}$ as a function of the Fermi energy obtained from the semiclassical calculation. We set the magnetic field $B = 10^{-5}\ \hbar/ea^2$ and the energy separation of the two Weyl points $\Delta E = 0.04\ v_F\hbar/a$.